

Application of gold nanoparticles–epoxy surface nanocomposites for controlling hotspot density on a large surface area for SERS applications

Attila Bonyár^{a,*}, Shereen Zangana^a, Tomáš Lednický^b, István Rigó^c, István Csarnovics^d, Miklós Veres^c

^a Department of Electronics Technology, Faculty of Electrical Engineering and Informatics, Budapest University of Technology and Economics, Budapest, Hungary

^b CEITEC - Central European Institute of Technology, Brno University of Technology, Brno, Czech Republic

^c Institute for Solid State Physics and Optics, Wigner Research Centre for Physics, Budapest, Hungary

^d Department of Solid State Physics, University of Debrecen, Debrecen, Hungary



ARTICLE INFO

Article history:

Received 18 May 2021

Received in revised form 2 September 2021

Accepted 3 September 2021

Keywords:

SERS substrates

Nanocomposite materials

Raman spectroscopy

DNA detection

ABSTRACT

The applicability of a novel gold–epoxy surface nanocomposite for surface-enhanced Raman scattering (SERS) is investigated. The nanocomposite consists of ellipsoidal nanoparticles in a hexagonal arrangement, where the average particle diameter (D_0) and interparticle gap (D) can be controlled in the 0.15–1.00 (D/D_0) range on a large surface area (several cm^2). Numerical simulations were used to estimate the SERS enhancement factors of substrates with five different particle arrangements. The fabricated substrates' surface was functionalized with 20 base-pair long double-stranded DNA molecules and the intensities of the characteristic Raman peaks related to DNA were used to quantify the substrate performance. It was proved that by optimizing the fabrication parameters and maximizing the interparticle coupling, the characteristic Raman intensities could be increased by more than 2.5 orders of magnitude.

© 2021 The Authors. Published by Elsevier B.V. This is an open access article under the CC BY license (<http://creativecommons.org/licenses/by/4.0/>).

1. Introduction

One of the most promising application areas of plasmonic noble metal nanoparticles is surface-enhanced Raman scattering (SERS), an ultrasensitive vibrational spectroscopy method that provides specific fingerprint information of analytes [1]. According to the widely accepted electrochemical enhancement mechanism, SERS enhancement can reach multiple orders of magnitude in the intense plasmon near-field around the excited particles. The field intensity and the spectral position of the LSPR (localized surface plasmon resonance) absorption peak are strongly dependent on the geometrical properties of the nanoparticle arrangements (e.g., particle shape, size and interparticle distance). For different Raman excitation wavelengths, these respective parameters should be optimized in order to maximize the achievable SERS enhancement with the nanostructures, which is the main effort and focus of many recent works [1–3]. It was also shown that the near-field intensities could be multiplied by utilizing coupling between the nanostructures and the resulting hotspots contribute significantly to the overall SERS enhancement. The

fact that decreasing the interparticle gap leads to an increased Raman intensity has been proven both experimentally and by simulations [4–6].

Since hotspot density is critical for SERS, one should consider it a primary criterion when choosing a SERS substrate for a given application. Generally, selecting a suitable technology for substrate fabrication is not trivial and usually requires many compromises. Top-down techniques, such as direct writing lithography (electron beam lithography [7] or focused ion beam lithography [8]), grant excellent control over the size and spacing of the nanostructures, but only on a limited surface area. Other deposition-based techniques might have poor control over the size/shape of the particles or have small nanostructure surface coverage [9,10]. Bottom-up techniques, such as wet chemical synthesis, also give reasonable control over the shape and size of the nanoparticles (e.g., spheres, rods, triangles, core–shell structures), but with the subsequent surface chemistry, it might be challenging to control the particle spacing [11,12]. Lately, attention has been turned towards nanocomposites [13] and template based-fabrication technologies (e.g., nanoimprint lithography [3, 14]) with which highly sensitive nanoparticle arrays could be fabricated on relatively large surface areas.

* Corresponding author.

E-mail address: bonyar@ett.bme.hu (A. Bonyár).

Recently, we introduced a novel gold–epoxy surface nanocomposite, which was successfully used as an LSPR sensor for nucleic acid detection [15]. The fabrication technology is based on preparing a nanobowled aluminium template, made by anodic oxidation and subsequent etching. The template's hexagonal structure is used to create ellipsoidal gold nanoparticles, retaining the same hexagonal pattern. The particles' size (diameter and thickness) and the interparticle gap can be tuned by controlling the gold thin film deposition and subsequent annealing parameters. After synthesis, the particle arrangement is transferred to the surface of a transparent epoxy substrate. The main advantages of these plasmonic nanocomposites, considering either LSPR or SERS applications, are the following. (1) The precise control over the shape, size and interparticle distance can be maintained on a large surface area (several cm^2) in a homogeneous way (see Supplementary Materials Figs. S1–S3). (2) Through these parameters, the substrates' plasmon absorption peak can be fine-tuned between 535–625 nm, enabling optimization of the Raman excitation wavelength. (3) The interparticle gap (D) and particle diameter (D_0) ratio (D/D_0) can be controlled in the 0.15–1.00 range, which provides a high hotspot density on the whole surface. (4) The nanoparticle arrangement is stable on the polymer surface in fluidic environments; the substrates are robust. (5) The substrates can be considered cost-effective due to the large surface area and the generally inexpensive fabrication technology.

The substrates' SERS performance was quantified by DNA sensing. A DNA molecular layer was bound to the gold nanoparticles in a protocol identical to label-free sensing scenarios with a thiolated single-stranded probe-DNA and a complementary target-DNA molecule. Sensitive quantification of DNA molecules is increasingly important in many fields, such as pathogen detection, environmental monitoring or disease diagnostics. SERS is an excellent candidate for a successful DNA detection platform and it can give an accurate signal with high sensitivity [16]. Recently, several studies utilized SERS substrates for label-free DNA detection [16,17], with sensitivity enabling even single-molecule detection [18]. Low DNA concentrations were also detected by using Rhodamine B (RB) as a Raman label [19]. Here, our aim was not to test the substrates for label-free DNA detection, we merely used DNA since the molecules' inherently small size and characteristic Raman peaks make them ideal target materials for quantifying SERS performance related to these application areas.

2. Materials and methods

2.1. SERS substrate fabrication

The fabrication technology of gold–epoxy nanocomposite substrates is presented in detail in our previous work, including the optimization of the technological parameters [15]. Here, only a short description of the main process steps is given, as presented in Fig. 1. In the first phase, a nanobowled aluminium template is formed by the controlled porous anodic oxidation of an aluminium sheet and the subsequent selective chemical etching of this porous anodic alumina (PAA) layer. In the second phase, the nanoparticles are created by solid-state dewetting (SSD), including the deposition of a gold thin film on the nanobowled template and its subsequent thermal annealing. The last phase is the transfer of the nanoparticle arrangement onto the surface of a transparent polymer substrate. This phase consists of polymer casting, aluminium template removal by chemical etching and the subsequent plasma etching of the polymer substrate to make the nanoparticles accessible.

The size and distribution (e.g., the interparticle gap) of the particles can be controlled in discrete steps by regulating the fabrication's parameters. The nanobowled aluminium template

fabrication was achieved by one-step anodizing. Two stable working points were chosen, both yielding hexagonally ordered cells, illustrated in Fig. 2 and referred to as type A and type B. For the type A template, an oxalic acid solution (0.3 M) was used at 7 °C with a potential of 40 V for 20 h; for the type B substrate, a sulphuric acid solution (0.3 M) was used at 0 °C with a potential of 25 V for 15 h. The control over the nanoparticles size was achieved by repeated thin-film deposition and annealing. Here, a precisely optimized film thickness is crucial for the desired nanoparticle formation. For type A substrates, the best results were achieved with subsequent layer depositions of 6 nm + 5 nm for A1 and A2 substrates, while for type B substrates, the optimal thickness was found to be 8 nm + 7 nm + 5.5 nm (B1, B2 and B3 substrates, respectively). The annealing temperature and time were 300 °C for 5 min in all cycles. To transfer the nanoparticle arrangement, a two-compound epoxy resin was used as a substrate (Elan-tron W 363 and EC 570, in a weight ratio of 100:33). After transfer, the polymer's surface was etched in a RIE chamber (PlasmaPro 80, Oxford Instruments Plasma Technology) in oxygen plasma for 40 s at a pressure of 6.7 Pa, power of 50 W and O_2 flow rate of 50 sccm. For a more detailed description of these processes, please see [15]. For imaging, a high-resolution scanning electron microscope (SEM, FEI Verios 460L) was used in the secondary electron (SE) mode with a 5 keV acceleration voltage.

2.2. SERS measurements

For Raman spectroscopy, a Renishaw InVia micro-Raman spectrometer was used. The wavelength of the laser source used for the excitation was 785 nm, with 100% power. The exposure time was 10 s with 5 accumulations. This wavelength is higher than the plasmonic absorption maxima of the substrate (between 535–625 nm [15]) and was selected to avoid any degradation of the epoxy substrate, which was previously observed with 532 nm and 633 nm excitations [20]. For the characterization of the surfaces, two measurement modes were used.

In the *normal mode*, the excitation spot has a diameter of ~ 1.8 μm , which was achieved by using a 50 \times objective (LWD50X, with $NA = 0.55$). The focus was set manually in this mode by monitoring the measured Raman intensities in a continuous acquisition mode and maximizing the signal intensities. In the *Z dimensional scan mode*, a Renishaw MS30 high speed encoded stage and a pinhole were used with a confocal depth profiling step size of 100 nm. After setting the focus (similarly to that described for the normal mode), spectra were obtained in the ± 15 μm range of this plane with 100 nm step resolution.

2.3. Surface functionalization

For the experiments, 20 base long probe-DNA and respective target-DNA molecules were purchased from Sigma-Aldrich (Germany). The complementary sequence is from the β -giardin gene of the parasite *Giardia lamblia* [21], which was previously tested by us for label-free sensing [15]. The DNA base sequences are the following (from 5' to 3'): probe-DNA: CGTACATCTTCTCCTTTT-[ThiC6]; target-DNA: AGGAAGAAGATGTACACCA. For surface functionalization, 1 μM probe and target DNA solutions were prepared in a buffer containing 0.75 M NaCl and 50 μM Na_2HPO_4 (pH 6.8). The same buffer was used to prepare the hybridization solution and also for rinsing the sample between each step. For cleaning the samples prior to DNA functionalization, 15 s low-power (20 W) O_2 plasma treatment was applied (at 0.4 mbar). Subsequently, the probe-DNA solution (1 μM) was drop coated on the sample surface. After an overnight DNA immobilization, 1 mM solution of MCH (dissolved in buffer) was used to remove

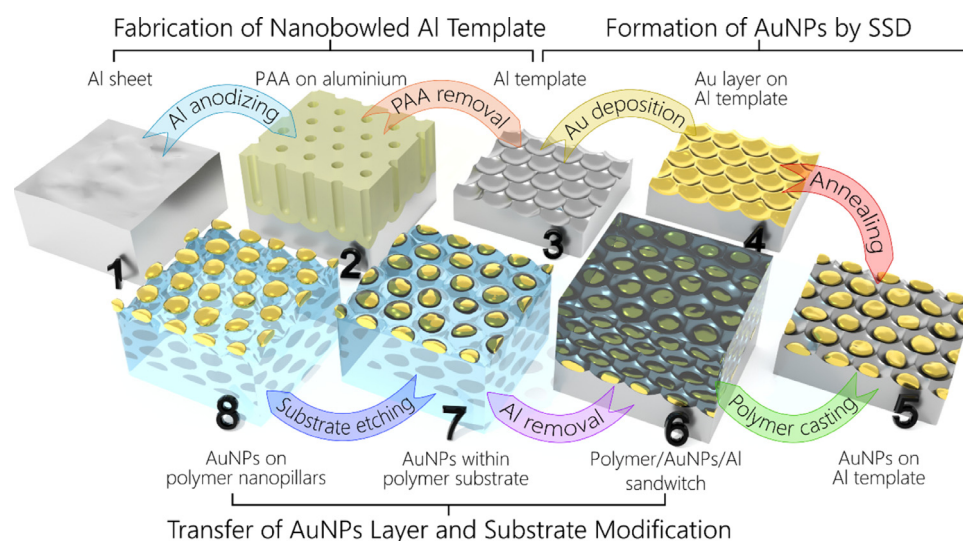


Fig. 1. The main fabrication steps of gold-epoxy nanocomposite SERS substrate preparation [15].

non-covalently bound DNA strands from the surface. DNA hybridization was performed for 2 h at RT from a 1 μM target-DNA solution. Before the Raman-spectroscopy measurements, only the buffer was used to rinse the substrates and all measurements were then performed in air. For data on the stability of the SERS substrates and recommendations for cleaning procedures, please see the Supplementary Materials Section 4.

2.4. Numerical simulations

The numerical simulations were performed with the MNPBEM (Metallic NanoParticle Boundary Element Method) MATLAB toolbox [22], which was explicitly developed to calculate the electric fields and optical properties of nanoparticles. Nano-spheroids in a hexagonal arrangement were used to model the nanoparticles arrays. The particles' size and interparticle gaps were determined based on SEM images ($>16 \mu\text{m}^2$). The spheroids were created from 144 vertices, and the 'retarded' solver was used to calculate the field intensities on the illuminated arrangement, which solves all the Maxwell equations on the surface elements. A plane-wave excitation was used at a wavelength of 785 nm. The propagation direction was normal to the plane of the particle arrangement. The wave was linearly polarized in the plane, having three components with polarization angles of 0, 60 and 120°, respectively. The electric field is calculated as the sum of these three excitation components.

3. Results and discussion

The SERS performance of five different Au-epoxy nanocomposite substrates – consisting of five different nanoparticle arrangements – was investigated experimentally and with numerical simulations. Fig. 2 presents SEM images of all five arrangements. The distribution of the particles is uniform on the whole fabrication area of around 2 cm^2 , as illustrated with additional SEM images in the Supplementary Materials (Fig. S1). The SEM images used to measure the size of the nanoparticles were obtained while the nanoparticle arrangement was still on the nanobowled aluminium template. For SEM images obtained after the transfer to the epoxy substrate, please see Fig. S2. The homogeneous purple colour of the completed surface nanocomposites also indicates a stable and uniform particle arrangement after the transfer, as can be seen in the photograph of Fig. S3.

As discussed in Section 2.1, by controlling the pore size and the deposited layer thickness, the size and interparticle distance of the spheroidal particles can be influenced. For type A substrates, the average size of the pores is $68 \pm 3 \text{ nm}$; for type B, it is $109 \pm 4 \text{ nm}$. The diameter of the resulting particles increases (denoted as D_0 and calculated as the equivalent circle diameter based on SEM images) with the first (A1, B1), second (A2, B2) and third (B3) deposition, and the annealing cycle. The histograms of the measured size distributions are given in Fig. 4a. Based on the TEM images, it was found that the thickness of the spheroids also scales with their mean diameter. The diameter/thickness ratios for the five arrangements were found to be 2.13 (A1), 1.73 (A2), 1.9 (B1), 1.7 (B2) and 1.4 (B3). The interparticle distances (D) were calculated as the difference between the average pore size and the particle diameter. These values were used to construct the models for the numerical simulations.

A generally accepted approach to compare achievable SERS enhancements with the electromagnetic field strength of the nanoparticles is the fourth power-law relation of Eq. (1); where SERS EF is the SERS enhancement factor, E is the magnitude of the electric field, λ is the wavelength of monochromatic illumination, r and θ are the polar coordinates, since the field strength is dependent on the position [23].

$$\text{SERS EF}(\lambda) = \frac{E(\lambda, r, \theta)^4}{E_0(\lambda, r, \theta)^4} \quad (1)$$

To correlate our SERS substrates' performance, namely, the intensity of the measured Raman peaks of DNA, a modified version of Eq. (1) was used. By using Eq. (2), the electric field is calculated around the particles up to a given distance (r_1) from their surface with BEM (boundary element method) simulations, as illustrated in Fig. 3c. As given in Eq. (2), the average field enhancement is calculated in 2D (in the plane of the nanoparticles) in the ($r_0 - (r_0 + r_1)$) range, where r_0 is the radius of the ellipsoid, and ($r_0 + r_1$) is the outer radius of the integral. For our calculations r_1 was selected as 7 nm to match the estimated length of the DNA molecules that cover the nanoparticles.

$$\text{SERS EF}(\lambda) = \frac{\int_0^{2\pi} \int_{r_0}^{r_0+r_1} \frac{E(\lambda, r, \theta)^4}{E_0(\lambda, r, \theta)^4} dr d\theta}{(r_0 + r_1)^2 \pi - r_0^2 \pi} \quad (2)$$

Fig. 3 presents the electric field enhancement, illustrated for type A substrates with the same average pore size (68 nm) but with different particle diameters (51 nm in Fig. 3a and 60 nm in

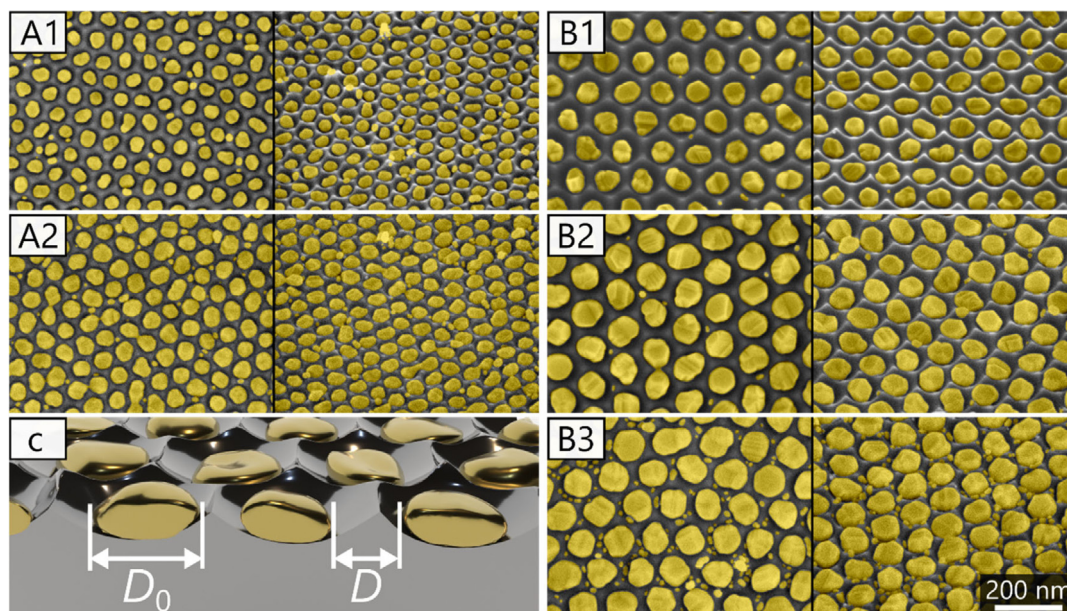


Fig. 2. SEM images (false colours) of top and tilt view (45°) presenting the size distribution of the five different nanoparticle array types. Image (c) illustrates the shape and position of the nanoparticles inside the nanobowls. The particle diameter will be referred to as D_0 , while the interparticle distance is denoted as D .

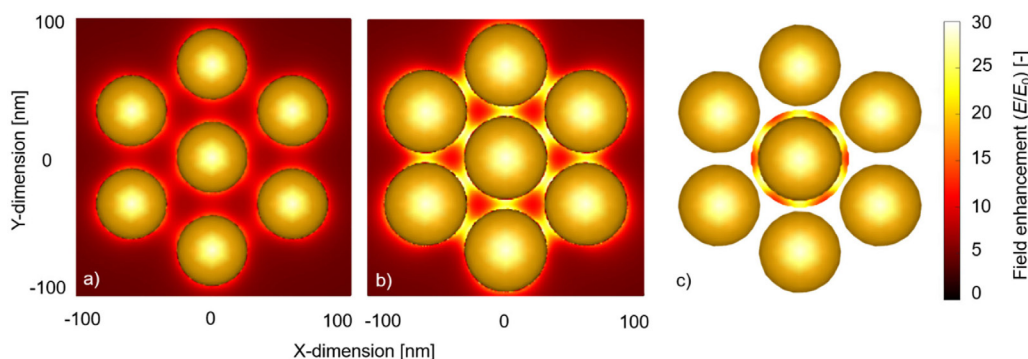


Fig. 3. Electric field enhancement (E/E_0) simulated with hexagonal nanoparticle arrangements. Unit cells and field enhancement for substrate type A with the same average pore size (68 nm) but with different particle diameters: 51 nm in (a) and 60 nm in (b) and (c). (c) Illustration of the 7 nm region, which was used for the calculations based on Eq. (2).

Figs. 3b and 3c). It can be seen that the interparticle plasmon coupling is properly excited with our plane-wave illumination and that a smaller interparticle distance results in a higher electric field enhancement, as expected. **Fig. 3c** illustrates the 7 nm region used to calculate the *SERS EF* based on Eq. (2). Additionally, the particle size distribution, given in **Fig. 4a**, was taken into consideration to estimate the response of our *SERS* substrates as precisely as possible. For this, the *SERS EF* was simulated and calculated based on Eq. (2) for all arrangements by changing the nanoparticles' size in the unit cell (**Fig. 3**) with 1 nm size resolution. The resulting *SERS EF* in the function of the dimensionless D/D_0 value is plotted in **Fig. 4c**. Narrowing the interparticle gap leads to an increasing electric field intensity and also an exponentially increasing *SERS EF*. This effect is a known trend, which was previously observed experimentally for other nanoparticle systems [4–6,24]. Based on **Fig. 4c**, the most intense enhancement starts below $D/D_0 < 0.3$, between 0.1 and 0.3, the *SERS EF* gains two orders of magnitude, from 10^4 to 10^6 . The trends are similar for all particle arrangements; however, larger particles with the same D/D_0 value (considering both diameter and thickness, which were scaled with the former) yield higher enhancements. An average *SERS EF* for the five different arrangements were obtained by considering the particles size distributions. These distributions

were implemented by calculating weight functions based on the histograms (**Fig. 4a**) and calculating a weighted average from **Figs. 4b and 4c**. The resulting values were 2.8×10^3 and 9×10^3 for A1 and A2, and 5.8×10^3 , 1.9×10^4 and 3.2×10^4 for B1, B2 and B3 type of substrates, respectively. Although these calculated *SERS* enhancements strongly correlate with the average interparticle gap between the particles, several factors that might influence their performance could not be considered. One is their irregular shape, which may form local hotspots with a lower than average interparticle distance. Based on **Fig. 4c**, this might significantly increase the *SERS EF*. The same is true for the small satellite nanoparticles squeezed between the bigger particles (evident in **Fig. 2** for substrate type B3). For these reasons, the actual *SERS EF* of the substrates might be expected to be higher than the estimated values. Conclusively, based on the simulations, significant differences can be expected from the substrates in terms of Raman peak intensity.

Figs. 5 and 6 present the obtained *SERS* spectra on the gold–epoxy nanocomposite substrates. The spectra shown in **Fig. 5** were obtained in the normal mode (as defined in Section 2.2) by manually focusing the laser spot on the substrate's surface. In **Fig. 5a**, the reference spectrum measured on the epoxy substrate is given (measured on substrate type A2), while **Fig. 5b** presents

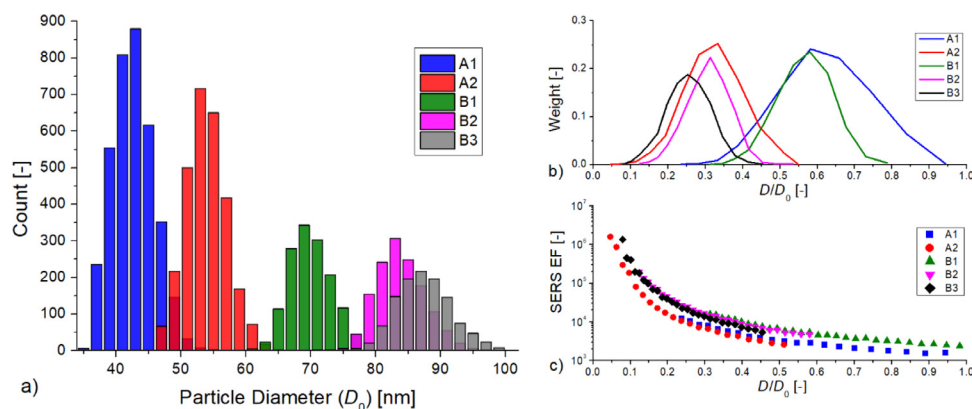


Fig. 4. (a) The distribution of particle diameters, measured based on SEM images. (b) Weight functions calculated from the histograms in (a), in the function of D/D_0 . (c) SERS EF obtained from the numerical simulations (calculated based on Eq. (2)), plotted in the function of D/D_0 .

the spectra after probe-DNA immobilization and after target-DNA hybridization. The repeatability of the SERS signal in various spots on one sample, both for bare epoxy and after DNA functionalization, is demonstrated in the Supplementary Materials (Figs. S4a and S4b). Spectra obtained on different types of SERS substrates are also compared here (Fig. S4c) and show good reproducibility between the substrate types.

In Fig. 5a, all the marked peaks correspond well to epoxy related peaks, in good accordance with the literature. Namely, 640 cm^{-1} is related to epoxy ring deformation, 822 cm^{-1} to $-\text{CH}$ wagging, 1113 cm^{-1} to epoxy ring deformation, 1460 cm^{-1} to $-\text{CH}_2$ deformation and 1610 cm^{-1} to aromatic ring stretching [25,26]. In Fig. 5b, the two spectra after DNA immobilization and hybridization differ significantly from the epoxy reference. Although some smaller peaks can be associated with the epoxy substrate (e.g., wide bumps around 650 and 1600 cm^{-1}), most are characteristic of the DNA. Based on the rich available data on the characteristic Raman peaks of DNA molecules [27–33], the most intense peaks can be assigned to the following vibrational modes (for a detailed collection of the identified peaks, please see Table S1 in the Supplementary Materials): $745\text{--}753\text{ cm}^{-1}$ for thymine stretching in C5-CH_3 ; $828\text{--}835\text{ cm}^{-1}$ for phosphodiester O-P-O stretching and thymine C4-C5 stretching (combined); $888\text{--}898$ and $925\text{--}935\text{ cm}^{-1}$ for deoxyribose C-C vibrations; $1021\text{--}1033\text{ cm}^{-1}$ for thymine C-N-C bending [27]. Several peaks can be assigned to purine bases (Guanine, Adenine), e.g., 1333 , 1361 , 1453 and 1484 cm^{-1} .

Although the investigation of the changes in the peak positions and intensities after DNA hybridization was not the primary focus of our research, we have to note that changes in these quantities can be expected due to the following reasons. In the case of a realistic DNA molecule (with multiple types of bases) the relative contribution of the bases in the total SERS spectrum depends on the position of the base relative to the hotspots on the surface and thus on the orientation of the DNA chains. The bases that are located in the highest E-field regions will contribute more to the overall spectrum. Since our probe-DNA is pyrimidine rich – 17 out of 20 bases are either T or C, as illustrated in Fig. 6a – and since the probe starts with a poly-T sequence (which is closest to the surface of the nanoparticles and thus is exposed to the highest field intensities), our spectra will always be dominated with thymine characteristic peaks, as can be seen in Fig. 5b and Figs. S4a-c. The binding of the target molecule can be either indicated by the increased intensity of DNA characteristic peaks (due to more bases and phosphate backbone) or by the appearance of purine base related peaks (since the target is purine-rich). Variance in the relative peak intensities can be expected due to local inhomogeneities in the DNA orientation. For further information

regarding the relative contribution of individual DNA bases in the Raman spectrum, please see [27,32,33].

Fig. 6 presents the Z scan mode results, measured on the same sample used for Fig. 5b, after target-DNA hybridization. In this mode, a pinhole was used, and the focal plane was scanned with a 100 nm step resolution (as discussed in Section 2.2). Initially, the laser spot was focused on the surface manually and then the scan was performed in a $\pm 15\text{ }\mu\text{m}$ range from this location in the normal direction. The detected intensity of the Raman peaks naturally varies by changing the focal plane. As shown in Fig. 6b, the intensity of the obtained spectra has a clear maximum in the function of the distance along the normal direction. The spectrum with the highest peak intensity is shown in Fig. 6a, and this point was selected as the arbitrary zero position in Fig. 6b to plot the intensity distribution of three selected peaks.

All selected peaks have a very sharp maximum in the same position along the normal direction. The full-width-at-half-maximum of this peak is $100\text{--}200\text{ nm}$ (keeping in mind the 100 nm step resolution of the scan). This value corresponds well with the estimated thickness of the nanoparticle arrangement, considering that the laser spot has a diameter of around $1\text{ }\mu\text{m}$ in this mode and that the average surface roughness (S_a) of the substrate was between $15\text{--}30\text{ nm}$ in a $1\text{ }\mu\text{m}^2$ area, with min-max distances below 150 nm (measured with AFM in a B3 type substrate). Based on this, it can be confirmed that the majority of the SERS signal originates from a very thin layer of space, corresponding to the plane of the particle arrangement, and in this plane, the DNA-related peaks are strong and well-defined. In Fig. 6b, the two peaks related to thymine (754 and 1021 cm^{-1}) yield nearly zero signal outside this focal plane, while the peak at 1333 cm^{-1} has some intensity originating from the substrate as well. This fluctuation in the 1333 cm^{-1} signal is probably due to overlapping $-\text{CH}_2$ vibrations (e.g., around 1 and $1.5\text{ }\mu\text{m}$ in Fig. 6b).

To compare the five substrate types and establish the relationship between their hotspot densities and their SERS performance, the maximum Raman intensities of the selected peaks were plotted against the calculated SERS EFs, calculated based on the numerical simulations. To compare the performance of the different substrates in the best possible way, the results obtained with the Z dimensional scan mode were used. In this mode, the highest signal intensity can be expected when the focal plane of the excitation beam exactly matches the plane of the particle arrangement, which eliminates the variance originating from manual focusing in the normal measurement mode. Thus, the maximal Raman intensity for a selected characteristic DNA peak was determined based on the Z scan results for each substrate type in the focal plane of the particle arrangement. The three characteristic peaks which were selected are thymine C5-CH_3

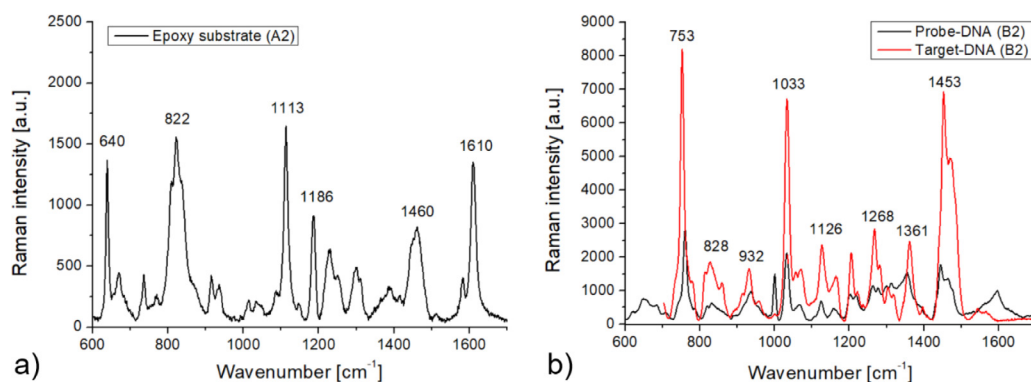


Fig. 5. SERS spectra illustrating peaks corresponding to (a) the epoxy substrate, measured on an A2 type substrate; (b) DNA molecules after probe-DNA immobilization and target binding, measured on a B2 type substrate. The spectra were obtained in the normal mode of the Raman spectrometer.

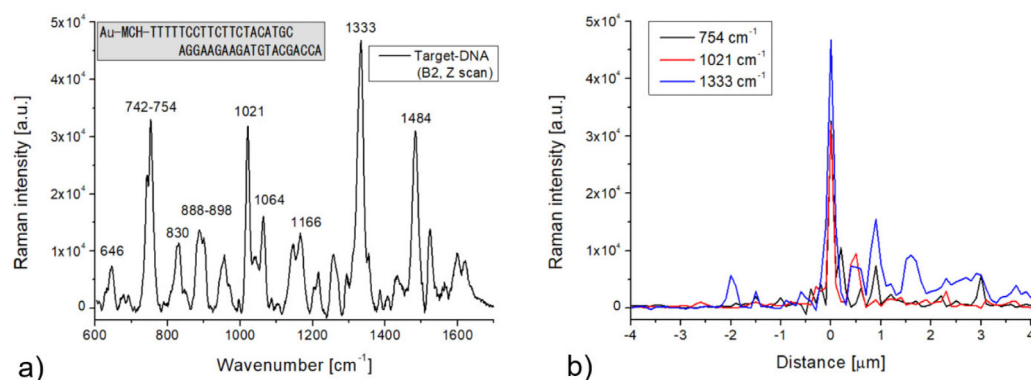


Fig. 6. (a) A SERS spectrum measured with the Z scan mode of the spectrometer on a B2 type substrate after target-DNA binding (corresponding to Fig. 4b, measured with the same sample). (b) Raman intensities of three characteristic peaks in the function of the focal plane's position. The step resolution was 100 nm, the plane with the highest intensity was chosen as the arbitrary zero position. The spectrum presented in (a) was measured at this plane.

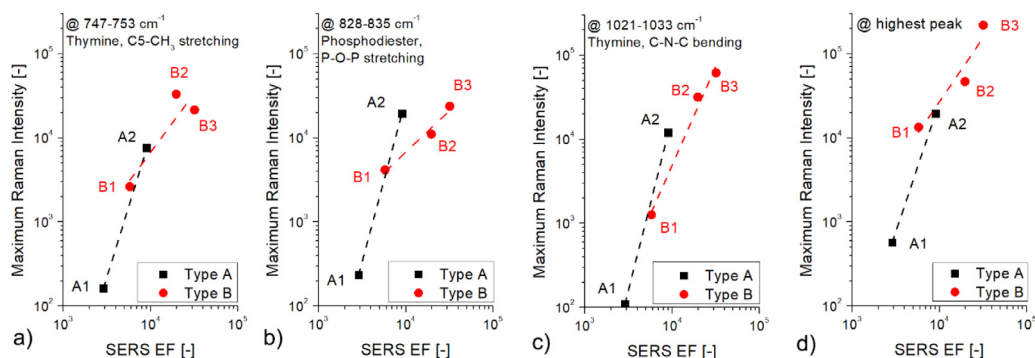


Fig. 7. The measured Raman peak intensities in the function of the SERS enhancement factors, which were calculated for the different substrate types/nanoparticle arrangements with BEM simulations. Graphs (a)-(c) corresponds to the maximal peak intensities for specific peaks, while (d) corresponds to the highest characteristic peak in each spectrum.

stretching (Fig. 7a), phosphodiester P-O-P stretching (Fig. 7b) and thymine C-N-C bending (Fig. 7c). In Fig. 7d, the intensity of each spectrum's highest DNA-related peak – obtained at the focal plane – is plotted against the SERS EF.

As can be seen in Fig. 7, the correlation between the obtained Raman intensities and the calculated SERS EFs is strong, especially for the thymine C-N-C bending (Fig. 7c) and the highest characteristic peak (Fig. 7d) plots. In Figs. 7a and 7b, slight variations can be observed, which can be considered natural, being caused by local inhomogeneities on the surface, the particle arrangement or in the DNA layer (e.g., its density or orientation). All of these can cause the relative SERS intensity of different DNA related peaks to vary from spot to spot.

The maximum difference between the Raman intensities obtained for different substrates can be more than 2.5 orders of magnitude, e.g., for the thymine C-N-C bending at 1021–1033 cm⁻¹, it was between 110 (a.u.) and 61600 (a.u.) for substrates A1 and B3, respectively. This measured Raman intensity difference is at least one order of magnitude smaller than the calculated max–min SERS EF difference: 2.8×10^3 and 3.2×10^4 for these same substrate types. It seems that the factors which were not considered for the simulation, namely the irregular shape and smaller satellite particles, could all contribute smaller interparticle gaps and thus higher SERS EFs, and these indeed play a significant part in determining the overall response of the substrates.

The presented results in Figs. 6 and 7 prove that the quality of the nanocomposite is suitable for SERS purposes and that the transfer of the nanoparticles to the polymer substrate and its subsequent etching (as discussed in Section 2.1. and illustrated in Fig. 1) results in a well-maintained arrangement both laterally and along the normal dimension. Fig. 6 shows that the particles are confined to a 100–200 nm thick layer, while Fig. 7 confirms that the designed interparticle gaps are retained after the transfer, and thus the hotspot density of the substrates can be controlled. All substrate types that have characteristic Raman intensities above 10^4 (a.u), e.g., A2, B2 and B3, could be used to investigate molecular layers and interactions with success.

4. Conclusions

The applicability of a novel gold–epoxy surface nanocomposite, consisting of ordered ellipsoidal gold nanoparticles in hexagonal arrangements, as highly sensitive and cost-effective SERS substrates was demonstrated. The characteristic peaks of a DNA monolayer were used to quantify the SERS performance of each substrate type. It was shown that by controlling the fabrication technology parameters, the interparticle gap, and thus the hotspot density of the arrangements, could be positively influenced. Using a Z-dimensional scanning spectroscopy mode and finding the focal plane of the particle arrangements, the obtained SERS intensities could be directly compared with numerical simulations, which aimed at estimating the SERS enhancement factor by calculating the electric field intensities. It was proven that the increased performance could be related to a smaller average interparticle distance and stronger interparticle coupling. By maximizing this effect, 2.5 orders of magnitude increase in the measured characteristic Raman intensities could be achieved. One of the proposed substrate's main strengths is that it can be prepared on a several cm^2 large surface area (with precise control over the particle arrangement on the whole surface), which can offer a cost-effective solution for many applications.

CRedit authorship contribution statement

Attila Bonyár: Conceptualization, Methodology, Software, Writing – original draft, Writing – review & editing, Visualization, Supervision. **Shereen Zangana:** Methodology, Investigation, Validation, Visualization. **Tomáš Lednický:** Methodology, Investigation, Visualization, Writing – review & editing. **István Rigó:** Methodology, Investigation, Validation. **István Csarnovics:** Conceptualization. **Miklós Veres:** Conceptualization, Writing – review & editing, Supervision.

Declaration of competing interest

The authors declare that they have no known competing financial interests or personal relationships that could have appeared to influence the work reported in this paper.

Acknowledgements

The research reported in this paper and carried out at the Budapest University of Technology and Economics has been supported by the NRD Fund (TKP2020 IES, Grant No. BME-IE-BIO) based on the charter of bolster issued by the NRD Office under the auspices of the Ministry for Innovation and Technology.

This work was supported by the VEKOP-2.3.2-16-2016-00011 grant, which is co-financed by the European Union and European Social Fund.

This work was partially supported by the Nanoplasmonic Laser Fusion Research Laboratory project financed by the National Research and Innovation Office (NKFIH) and by the Eotvos Roland Research Network (ELKH), Hungary.

The CzechNanoLab project LM2018110 funded by MEYS CR is gratefully acknowledged for the financial support of the measurements/sample fabrication at CEITEC Nano Research Infrastructure.

Appendix A. Supplementary data

Supplementary material related to this article can be found online at <https://doi.org/10.1016/j.nanos.2021.100787>.

References

- [1] Shinki, S. Sarkar, Au_{0.5}Ag_{0.5} Alloy nanolayer deposited on pyramidal Si arrays as substrates for surface-enhanced Raman spectroscopy, *ACS Appl. Nano Mater.* 3 (7) (2020) 7088–7095, <http://dx.doi.org/10.1021/acsnano.0c01407>.
- [2] P. Pal, A. Bonyár, M. Veres, L. Himics, L. Balázs, L. Juhász, I. Csarnovics, A generalized exponential relationship between the surface-enhanced Raman scattering (SERS) efficiency of gold/silver nanoisland arrangements and their non-dimensional interparticle distance/particle diameter ratio, *Sens. Actuat. A* 314 (2020) 112225, <http://dx.doi.org/10.1016/j.sna.2020.112225>.
- [3] V. Suresh, L. Ding, A.B. Chew, F.L. Yap, Fabrication of large-area flexible SERS substrates by nanoimprint lithography, *ACS Appl. Nano Mater.* 1 (2) (2018) 886–893, <http://dx.doi.org/10.1021/acsnm.7b00295>.
- [4] G. Liu, K. Li, Y. Zhang, J. Du, S. Ghafoor, Y. Lu, A facile periodic porous Au nanoparticle array with high-density and built-in hotspots for SERS analysis, *Appl. Surf. Sci.* 527 (2020) 146807, <http://dx.doi.org/10.1016/j.apsusc.2020.146807>.
- [5] V.T.N. Linh, J. Moon, C.W. Mun, V. Devaraj, J.-W. Oh, S.-G. Park, D.-H. Kim, J. Choo, Y.-I. Lee, H.S. Jung, A facile low-cost paper-based SERS substrate for label-free molecular detection, *Sensors Actuators B* 291 (2019) 369–377, <http://dx.doi.org/10.1016/j.snb.2019.04.077>.
- [6] Z. Zhu, T. Zhu, Z. Liu, Raman scattering enhancement contributed from individual gold nanoparticles and interparticle coupling, *Nanotechnology* 15 (3) (2004) 357–364, <http://dx.doi.org/10.1088/0957-4484/15/3/022>.
- [7] Z.-Q. Tian, B. Ren, Infrared and Raman spectroscopy in analysis of surfaces, *Encycl. Anal. Chem.* (2006) 1–40, <http://dx.doi.org/10.1002/9780470027318.a2516>.
- [8] X. Zhang, J. Zhao, A.V. Whitney, J.W. Elam, R.P. Van Duyne, Ultrastable substrates for surface-enhanced Raman spectroscopy: Al₂O₃ overlayers fabricated by atomic layer deposition yield improved anthrax biomarker detection, *J. Am. Chem. Soc.* 128 (31) (2006) 10304–10309, <http://dx.doi.org/10.1021/ja0638760>.
- [9] J. Theiss, P. Pavaskar, P.M. Echternach, R.E. Muller, S.B. Cronin, Plasmonic nanoparticle arrays with nanometer separation for high-performance SERS substrates, *Nano Lett.* 10 (8) (2010) 2749–2754, <http://dx.doi.org/10.1021/nl904170g>.
- [10] J.T. Bahns, A. Imre, V.K. Vlasko-Vlasov, J. Pearson, J.M. Hiller, L.H. Chen, U. Welp, Enhanced Raman scattering from focused surface plasmons, *Appl. Phys. Lett.* 91 (8) (2007) 081104, <http://dx.doi.org/10.1063/1.2759985>.
- [11] M. Rycenga, C.M. Cobley, J. Zeng, W. Li, C.H. Moran, Q. Zhang, D. Qin, Y. Xia, Controlling the synthesis and assembly of silver nanostructures for plasmonic applications, *Chem. Rev.* 111 (6) (2011) 3669–3712, <http://dx.doi.org/10.1021/cr100275d>.
- [12] P.Z. El-Khoury, E. Khon, Y. Gong, A.G. Joly, P. Abellan, J.E. Evans, N.D. Browning, D. Hu, M. Zamkov, W.P. Hess, Electric field enhancement in a self-assembled 2D array of silver nanospheres, *J. Chem. Phys.* 141 (21) (2014) 214308, <http://dx.doi.org/10.1063/1.4902905>.
- [13] J. Fang, J. Zhu, M. Fu, Y. Gu, G. Li, H. Hou, Z. Lin, X. Chen, X. Li, A SERS substrate with remarkable reproducibility: Adsorbing and detecting both hydrophobic and hydrophilic molecules using rGO/PEI/PAA/CD-agnp nanocomposites, *Appl. Surf. Sci.* 542 (2021) 148708, <http://dx.doi.org/10.1016/j.apsusc.2020.148708>.
- [14] J. Cai, Z. Wang, M. Wang, D. Zhang, Au nanoparticle-grafted hierarchical pillars array replicated from diatom as reliable SERS substrates, *Appl. Surf. Sci.* 541 (2021) 148374, <http://dx.doi.org/10.1016/j.apsusc.2020.148374>.
- [15] T. š. Lednický, A. Bonyár, Large scale fabrication of ordered gold nanoparticle–epoxy surface nanocomposites and their application as label-free plasmonic DNA biosensors, *ACS Appl. Mater. Interfaces* 12 (4) (2020) 4804–4814, <http://dx.doi.org/10.1021/acsnami.9b20907>.
- [16] L. Bi, Y. Rao, Q. Tao, J. Dong, T. Su, F. Liu, W. Qian, Fabrication of large-scale gold nanoplate films as highly active SERS substrates for label-free DNA detection, *Biosens. Bioelectron.* 43 (2013) 193–199, <http://dx.doi.org/10.1016/j.bios.2012.11.029>.

- [17] O. Gusebnikova, P. Postnikov, A. Pershina, V. Svorcik, O. Lyutakov, Express and portable label-free DNA detection and recognition with SERS platform based on functional Au grating, *Appl. Surf. Sci.* 470 (2019) 219–227, <http://dx.doi.org/10.1016/j.apsusc.2018.11.092>.
- [18] X. Gao, H. Zhang, X. Fan, C. Zhang, Y. Sun, C. Liu, Z. Li, S. Jiang, B. Man, C. Yang, Toward the highly sensitive SERS detection of bio-molecules: the formation of a 3D self-assembled structure with a uniform GO mesh between Ag nanoparticles and Au nanoparticles, *Opt. Express* 27 (18) (2019) 25091, <http://dx.doi.org/10.1364/oe.27.025091>.
- [19] C. Fang, A. Agarwal, K.D. Buddharaju, N.M. Khalid, S.M. Salim, E. Widjaja, M.V. Garland, N. Balasubramanian, D.-L. Kwong, Dna detection using nanostructured SERS substrates with Rhodamine B as Raman label, *Biosens. Bioelectron.* 24 (2) (2008) 216–221, <http://dx.doi.org/10.1016/j.bios.2008.03.032>.
- [20] S. Zangana, T. Lednický, I. Rigo, I. Csarnovics, M. Veres, A. Bonyár, Surface-enhanced Raman spectroscopy investigation of DNA molecules on gold/epoxy nanocomposite substrates, in: 2020 IEEE 26th International Symposium for Design and Technology in Electronic Packaging (SIITME), 2020, pp. 32–36, <http://dx.doi.org/10.1109/siitme50350.2020.9292267>.
- [21] R.A. Guy, C. Xiao, P.A. Horgen, Real-time PCR assay for detection and genotype differentiation of giardia lamblia in stool specimens, *J. Clin. Microbiol.* 42 (7) (2004) 3317–3320, <http://dx.doi.org/10.1128/JCM.42.7.3317-3320.2004>.
- [22] U. Hohenester, A. Trügler, MNPBEM – A matlab toolbox for the simulation of plasmonic nanoparticles, *Comput. Phys. Comm.* 183 (2) (2012) 370–381, <http://dx.doi.org/10.1016/j.cpc.2011.09.009>.
- [23] Pilot, Signorini, Durante, Orian, Fabris Bhamidipati, A review on surface-enhanced Raman scattering, *Biosensors* 9 (2) (2019) 57, <http://dx.doi.org/10.3390/bios9020057>.
- [24] A. Bonyár, I. Csarnovics, M. Veres, L. Himics, A. Csik, J. Kámán, L. Balázs, S. Kökényesi, Investigation of the performance of thermally generated gold nanoislands for LSPR and SERS applications, *Sensors Actuators B* 255 (2018) 433–439, <http://dx.doi.org/10.1016/j.snb.2017.08.063>.
- [25] A. Katunin, K. Krukiewicz, R. Turczyn, Evaluation of residual cross-linking caused by self-heating effect in epoxy-based fibrous composites using Raman spectroscopy, *Chem. Sci. Tech. Mark.* 68 (11) (2014) 957–966.
- [26] H. Vašková, V. Kresálek, Quasi real-time monitoring of epoxy resin crosslinking via Raman microscopy, *Int. J. Math. Models Methods Appl. Sci.* 5 (7) (2011) 1197–1204.
- [27] D.M. Sagar, L.E. Korshoj, K.B. Hanson, P.P. Chowdhury, P.B. Otoupal, A. Chatterjee, P. Nagpal, High-throughput block optical DNA sequence identification, *Small* 14 (4) (2017) 1703165, <http://dx.doi.org/10.1002/sml.201703165>.
- [28] J. Kim, H.J. Park, J.H. Kim, B. Chang, H.-K. Park, Label-free detection for a DNA methylation assay using Raman spectroscopy, *Chin. Med. J.* 130 (16) (2017) 1961–1967, <http://dx.doi.org/10.4103/0366-6999.211874>.
- [29] A.J. Ruiz-Chica, On the interpretation of Raman spectra of 1-aminooxy-spermine/DNA complexes, *Nucleic Acids Res.* 32 (2) (2004) 579–589, <http://dx.doi.org/10.1093/nar/gkh232>.
- [30] A. AW, T. JC, Double-stranded DNA damage assessed with Raman spectroscopy, *Biochem. Anal. Biochem.* 5 (3) (2016) 284, <http://dx.doi.org/10.4172/2161-1009.1000284>.
- [31] A. De Angelis, M.A. Ferrara, G. Di Caprio, S. Managò, L. Sirleto, G. Coppola, A.C. De Luca, Spermatozoa quality assessment: a combined holographic and Raman microscopy approach, in: *Optical Methods for Inspection, Characterization, and Imaging of Biomaterials II*, 2015, <http://dx.doi.org/10.1117/12.2186393>.
- [32] A. Barhoumi, D. Zhang, F. Tam, N.J. Halas, Surface-enhanced Raman spectroscopy of DNA, *J. Am. Chem. Soc.* 130 (16) (2008) 5523–5529, <http://dx.doi.org/10.1021/ja800023j>.
- [33] C. Otto, T.J.J. van den Tweel, Surface-enhanced Raman spectroscopy of DNA bases, *J. Raman Spectrosc.* (1986) <http://dx.doi.org/10.1002/JRS.1250170311>.